Development of novel MOG analogues with increased stability to explore MCT2 and α-ketoglutarate biology *in vivo*

Louise Fets[1,4], Patrícia M. Nunes[1], Sebastien Campos[2], Mariana Silva dos Santos[3], Natalie Bevan[1], Emma Sherriff[2], James I. MacRae[3], David House[2], Dimitrios Anastasiou[1*]

[1]Cancer Metabolism Laboratory, Francis Crick Institute, UK; [2]Crick–GSK Biomedical LinkLabs, UK; [3]Metabolomics Science Technology Platform, Francis Crick Institute, UK; [4]Present address: Drug Transport and Tumour Metabolism Lab, MRC London Institute of Medical Sciences, UK

[*]*Corresponding author*

ABSTRACT

α-ketoglutarate (αKG) is a central metabolic node with far-reaching influence on cellular physiology. The αKG analogue *N*-oxalylglycine (NOG) and its membrane-permeable pro-drug derivative dimethyloxalylglycine (DMOG) have been broadly used as tool compounds both *in vitro* and *in vivo* to study αKG-dependent processes. In cell culture media, DMOG is rapidly converted to MOG, a substrate of the monocarboxylate transporter MCT2. The expression level of MCT2 determines the intracellular concentration of NOG, and, as such, influences the molecular targets NOG engages with. Here we show that DMOG and MOG are highly unstable also in mouse blood. We therefore designed and characterised a series of MOG analogues with two aims: to improve pharmacokinetic properties, and to explore the pharmacophore of MCT2, a relatively understudied member of the SLC16 family. We report MOG analogues that maintain MCT2-dependent uptake, including NOG-generating compounds that replicate the metabolic effects of MOG in a concentration-dependent manner. One such analogue, IPOG, shows significantly increased blood stability, and an improved overall pharmacokinetic profile, leading to increased NOG accumulation in MCT2-expressing tumours versus isogenic controls.

KEYWORDS

Dimethyl-oxalylglycine (DMOG), methyl-oxalylglycine (MOG), *N*-oxalylglycine (NOG), monocarboxylate transporter 2 (MCT2), *SLC16A7*, α-ketoglutarate, prolyl hydroxylases, transporter-mediated drug uptake, structure-activity relationship.

INTRODUCTION

The study of metabolism has long been aided by the use of metabolite analogues that allow the rapid and reversible inhibition of enzymes and pathways in different experimental settings[1]. In the field of cancer metabolism, analogue compounds such as 2-deoxyglucose, 6-diazo-5-oxo-L-norleucine (DON) and dichloroacetate (DCA) continue to complement genetic approaches to dissect the strengths and vulnerabilities associated with oncogene-driven metabolic changes in tumours[2–4]. Metabolite analogues are also among some of the most important clinically used chemotherapeutic compounds: from gemcitabine and 5-fluoro-uracil (5-FU), nucleoside analogues used as therapies in pancreatic and colorectal cancer; to methotrexate and pemetrexed, folate analogues administered to treat a range of malignancies[5,6]. The development and refinement of metabolite analogues for *in vivo* studies therefore provides valuable tools to facilitate improved mechanistic understanding of both metabolism and tumorigenesis.

α-ketoglutarate (αKG) is a key metabolic node and understanding its complex biology has been significantly facilitated by the structural analogue *N*-oxalylglycine (NOG), which has been extensively used *in vitro* along with its cell-permeable derivative, dimethyl-oxalylglycine (DMOG), to inhibit a range of αKG-dependent enzymes[7–9]. Most commonly, DMOG is utilised to elicit hypoxia signalling by inhibiting prolyl hydroxylase domain (PHD) enzymes leading to stabilisation of the transcription factor Hypoxia Inducible Factor 1α (HIF1α)[8,10]. HIF1α stabilisation is a therapeutic aim in conditions ranging from ischaemia and anaemia to inflammatory diseases[11,12], and previous studies using DMOG have demonstrated the potential benefits of inhibiting PHDs to achieve these goals[13,14].

As well as being a cofactor for αKG-dependent enzymes, αKG is also the entry point for glutamine carbons into the TCA cycle, a substrate for a large number of transaminase reactions, and has also been shown to influence mechanistic target of rapamycin (mTOR) activity[15]. Through regulation of ten-eleven translocation (TET) hydroxylases and Jumonji demethylases, αKG can modify epigenetic profiles during development[9] and in pathogenic contexts[16]. Additionally, through an as-yet unclear mechanism, αKG can influence aging[17], highlighting that there is still much to be discovered about the physiological functions of this metabolite.

DMOG is selectively toxic to some cancer cell lines, in a manner that strongly correlates to the expression level of the monocarboxylate transporter MCT2[18]. DMOG is unstable in cell culture media and is non-enzymatically converted to the monocarboxylate methyl-oxalylglycine (MOG) with a half-life of 10 min. MOG is a substrate for MCT2, the expression of which determines the concentration of NOG that accumulates intracellularly

72 ($[NOG]_{IC}$). In cells with high MCT2 expression, $[NOG]_{IC}$ can reach millimolar levels sufficient
73 to engage low-affinity αKG-binding enzymes such as isocitrate dehydrogenase (IDH) and
74 glutamate dehydrogenase (GDH) to severely disrupt metabolism and cause cytotoxicity.
75 DMOG has been extensively used *in vivo* for pre-clinical studies where, typically, it is
76 administered at concentrations that far exceed those required to inhibit the intended
77 intracellular targets[11,19,20]. Instability as a result of chemical or enzymatic de-esterification and
78 a subsequent loss of cell-permeability could explain the disparity in potency observed between
79 *in vitro* (purified enzyme) and *in vivo* studies, particularly in light of the high level of esterase
80 activity in blood. In support of this hypothesis, here we show that, in mouse blood, DMOG
81 degradation leads to a transient accumulation of MOG, which is rapidly converted to NOG.
82 With the aim of generating a more stable compound for *in vivo* exploration of αKG biology, we
83 designed and characterised a series of MOG analogues, identified those that recapitulate the
84 metabolic effects of MOG in cells, and then tested them in mice. The creation of a range of
85 analogues additionally enabled us to explore the pharmacophore of MCT2 ligands and thereby
86 increase understanding of this lesser-studied member of the *SLC16* transporter family.
87
88 **RESULTS**
89 *Design and synthesis of MOG analogues*
90 Given its relative instability in cell culture media[18] we reasoned that DMOG, and its
91 derivative MOG, may also have a short half-life *in vivo* (Fig. 1a). To test this idea, we examined
92 DMOG stability in whole mouse blood using liquid chromatography-mass spectrometry (LC-
93 MS) and found that it was almost instantaneously converted to MOG, with a half-life of less
94 than 1 min. (Fig. 1b). The MOG formed did not accumulate and was rapidly de-esterified to
95 NOG, with a half-life of 4 min. Synthetic MOG, which only contains the glycinate methyl ester
96 group, was converted to NOG (Fig. 1c) with a half-life mirroring the conversion of DMOG-
97 derived-MOG to NOG, suggesting that the oxoacetate methyl group of DMOG is lost first and
98 more rapidly, followed by the glycinate methyl group. The half-lives of these compounds in
99 mouse blood are significantly shorter than those previously measured in aqueous solution[18],
100 which we attribute to the well-documented high level of blood esterase activity.
101 Low stability of DMOG or MOG in blood prevented further well-controlled studies with
102 either compound *in vivo*. In order to overcome these issues, we designed a number of MOG
103 analogues, with two main objectives. Our first and major aim was to improve compound
104 stability while maintaining the ability to produce NOG intracellularly, in order to improve the *in*
105 *vivo* utility of this compound. Secondly, since MOG is a substrate for MCT2, by generating a
106 chemically diverse range of analogues, we aimed to broaden understanding of the chemical
107 space accommodated by this transporter.

108 We initiated our compound design using MOG as a chemical scaffold (**1,** Fig. 1a).
109 Based on our previous findings and the fact that esters are typically used as pro-drugs for
110 poorly absorbed carboxylic acid drugs,[21–24] we focused on the methyl ester of MOG as the
111 primary cause of compound instability in plasma. Furthermore, as the pharmacophore
112 required for MCT2-driven transport is unknown, substitutions were kept relatively
113 conservative. Therefore, we replaced the glycinate ester on MOG with i) bulkier alkyl esters
114 such as ethyl or isopropyl (compounds **2**-**3**), ii) esters possessing methyl substituents at the α
115 position (compounds **4**-**6**), iii) a ketone (compound **7**), or iv) 5-membered aromatic
116 heterocycles (compounds **8-10**). Importantly, compounds **1**-**6** are predicted to be de-esterified
117 to form NOG or methyl-substituted NOG, and therefore able to engage intracellular targets for
118 functional studies.
119 Esters **2** and **3** were designed to minimally increase the steric hindrance of the ester
120 substituent, which, would be expected to increase both chemical and metabolic stability[25–29].
121 We also explored branched esters (**4**-**6**), as substitutions on the α-carbon can increase
122 chemical stability[30] and cellular esterases can exhibit surprising selectivity toward complex
123 esters[31–33]. Ketones and amides (**7**) are classical ester isosteres[34], with the amide typically
124 used to improve the stability of drugs[35]. Notably, such small changes can have a significant
125 effect on the binding affinity of the compounds to their targets[36]. Finally, 5-membered ring
126 heterocycles, such as oxadiazoles (**10**) or oxazoles (**8**), have also been successfully used as
127 ester bioisosteres[37–40].
128
129 *MCT2-dependent uptake is maintained by a subset of MOG analogues*
130 To determine the MCT2-dependence of MOG analogue uptake into cells, we utilised
131 HCC1569 cells, a human breast cancer line that expresses very low levels of MCT2 and is
132 naturally resistant to MOG-induced toxicity[18]. We compared compound uptake in these cells
133 transduced with a control 'empty vector' plasmid (HCC1569-EV) to an isogenic line expressing
134 exogenous MCT2 (HCC1569-MCT2) (Fig. 2a, b). After incubation of both cell lines with each
135 analogue for 4 h, all tested compounds or derivatives thereof could be detected intracellularly.
136 In the case of compounds **7**-**10**, we detected the intact parent compound, however, as
137 expected, compounds **1**-**6** were all de-esterified intracellularly and therefore in these cases
138 we quantified NOG, or the NOG analogues that were formed. Intracellular accumulation of
139 these compounds occurred to varying extents, with the bulkier alkyl esters (compounds **2** and
140 **3**) and α-methyl substituents (compounds **4**-**6**) reaching concentrations in the millimolar range
141 (Fig. 2c). The de-esterification of these compounds within cells further decreases their
142 membrane permeability, which could effectively trap them inside cells and may explain the

143 higher concentrations observed. We defined MCT2-dependent uptake as a two-fold increase
144 in compound accumulation in HCC1569-MCT2 cells compared with HCC1569-EV cells[41]. The
145 MCT2-dependence of uptake varied between groups, but was maintained in both of the bulkier
146 alkyl esters (with the fold-change in uptake of compound **2** equivalent to MOG), as well as in
147 all 3 of the 5-membered aromatic heterocycles (compounds **8-10**, Fig. 2d). Although there was
148 a modest increase in the uptake of the α-methyl and ketone analogues in MCT2-expressing
149 cells compared to controls, these compounds did not meet the two-fold cut off criterion and so
150 were not further studied.
151
152 *MCT2-dependent analogues replicate the effects of MOG in a NOG-concentration dependent*
153 *manner*
154 MOG inhibits cell proliferation and leads to apoptosis in MCT2-expressing cells by
155 disrupting metabolism[18]. To test the relative efficacy of the bulkier alkyl esters and 5-
156 membered aromatic heterocycles in eliciting metabolic changes and death in cells, we first
157 assayed their effect on cell proliferation at varying concentrations, utilising our
158 HCC1569±MCT2 cell model. Over 96 h, MOG inhibited cell mass accumulation in a
159 concentration-dependent manner. This inhibition was markedly higher in MCT2-expressing
160 cells and was associated with increased $[NOG]_{IC}$ and increased apoptosis (Fig. 3a). The
161 bulkier alkyl esters (**2**,**3**) were also capable of slowing cell proliferation in a manner
162 proportional to the observed $[NOG]_{IC}$ achieved after dosing with these compounds (Fig. 3b).
163 Aligned with this observation, only the highest concentrations of compounds **2** and **3** were
164 able to increase apoptosis in MCT2-expressing cells. The 5-membered aromatic heterocycles
165 (**8-10**) did not affect proliferation of cells, either in the presence or absence of MCT2, except
166 in the case of compound **9**, where the highest dose led to a small decrease in proliferation
167 and a concomitant increase in apoptosis.
168 The most common use of DMOG as a tool compound is to inhibit PHDs and thereby
169 promote the accumulation of the transcription factor HIF1α. Similar to the effects observed on
170 cell growth and apoptosis, after 4 h of treatment with 1 mM of each analogue (the
171 concentration commonly used for treatment of cells with DMOG) either of the alkyl esters (**2**,
172 **3**), which produce NOG intracellularly, but not the aromatic heterocycles (**8-10**), induced
173 HIF1α stabilisation (Fig. 3c) in a $[NOG]_{IC}$-dependent manner.
174
175 *A subset of metabolic effects of MOG are maintained by the bulkier alkyl ester analogues*
176 As well as inhibiting prolyl hydroxylases, upon MCT2-driven accumulation to high
177 concentrations, NOG is able to engage other, lower-affinity αKG-binding enzymes. The effects
178 of MOG treatment on metabolism are rapid and extensive, and at high $[NOG]_{IC}$, targets include

αKG-binding enzymes GDH and IDH[18]. Inhibition of these targets can be determined by monitoring levels of the citrate m+4 and m+5 isotopologues derived from glutamine uniformly labelled with ^{13}C ([U^{13}C]-glutamine). Citrate m+4 is formed from the oxidative use of glutamine carbons in the canonical TCA cycle (Fig. 3d), and decreases as a result of GDH inhibition by NOG[18]. Citrate m+5 is produced by the reductive carboxylation of αKG by IDH (Fig. 3d). Reductive carboxylation is important in a range of physiological and pathological settings, including cancer, to enable the use of glutamine-derived carbons for the production of fatty acids, and to maintain redox balance[42–45].

We analysed the metabolism of HCC1569±MCT2 cells treated for 4 h with MOG analogues in the presence of [U-^{13}C]-glutamine. The depletion of TCA metabolites that had previously been observed after MOG treatment was partially recapitulated by compounds **2** and **3**, again in a $[NOG]_{IC}$ -dependent manner (Fig. 3e). Citrate m+5 was significantly decreased after treatment with either of the bulkier alkyl esters (**2**, **3**), whereas citrate m+4 was not (Fig. 3f), in line with the fact that IDH is inhibited by lower $[NOG]_{IC}$ than GDH[18]. These data therefore demonstrate that bulky alkyl ester MOG analogues are able to disrupt reductive carboxylation independently of effects on the oxidative TCA cycle. This differential inhibition of IDH and GDH relative to the $[NOG]_{IC}$ is reflective of their relative *in vitro* K_d values[18,46] and is consistent with our previous findings[18].

As expected, the 5-membered aromatic heterocycles (**8**-**10**, which do not form NOG) had no effect on the concentrations of TCA intermediates. One of the other key metabolites affected by MOG is α-glycerophosphate (αGP). Interestingly, even in DMSO-treated cells, a modest increase in αGP was observed in the MCT2-expressing cells suggesting that this transporter may lead to some alteration of cellular metabolism in HCC1569 cells (Fig. 3d). However, even relative to the MCT2-dependent increase, αGP levels were more than doubled after MOG treatment, with modest potentiation also seen with compounds **2**, **3** and **9** (Supplementary Fig. 1a).

Together, our data showed that compounds **2** and **3** entered cells and recapitulated the metabolic effects of MOG, in a manner that was proportional to the $[NOG]_{IC}$. We therefore chose to examine the stability of these two compounds in mice to enable more in-depth *in vivo* studies.

Higher alkyl ester analogues of MOG have improved pharmacokinetic profile

To test whether the alkyl ester substitutions changed stability for *in vivo* use, we measured the conversion of compounds **2** and **3** to NOG in mouse whole blood. In blood, the half-life of compound **2** was marginally lower than that of MOG (95% confidence intervals (CI) of 2.27-2.96 min and 3.01-3.69 min, respectively), however, compound **3** had a half-life of 14.4

215 min (95% CI = 10.18-21.24 min), a 4-fold improvement in blood stability compared with MOG
216 (Fig. 4a). As predicted, the three aromatic heterocycles were all stable in blood
217 (Supplementary Fig. 2a).
218 Based on its improved stability in blood, we decided to further characterise compound
219 **3** to better understand its pharmacokinetic and distribution profile. After intra-peritoneal (i.p.)
220 injection at 100 mg/kg into *Nod* SCID gamma (NSG) mice, the measured blood concentration
221 of the intact analogue was higher in compound **3**-dosed animals at both 15 and 60 min post-
222 injection than in MOG-dosed animals, with a corresponding increase in exposure (Fig. 4b). In
223 a small number of animals examined after 2 hours post-injection with MOG or (**3**) most NOG
224 was found in the liver and kidney, the two major sites of drug metabolism and excretion, with
225 lower levels observed in the spleen and at detectable, albeit very low, levels in heart, skeletal
226 muscle and brain (Supplementary Fig. 2b).
227 Since compound **3** demonstrated an improved pharmacokinetic profile relative to
228 MOG, it was taken forward into *in vivo* studies, and will henceforth be referred to as isopropyl-
229 oxalylglycine (IPOG).
230
231 *MCT2-dependent transport of IPOG* in vivo
232 To explore the utility of IPOG for *in vivo* experiments, we tested whether it would
233 selectively accumulate in MCT2-expressing tumours. To this end, we established an
234 orthotopic xenograft assay in which HCC1569 cells±MCT2, were injected into mammary fat
235 pads on opposing flanks of female NSG mice (Fig. 5a). Tumours grew slowly, as previously
236 reported[47], and there was no significant difference between the size of tumours from
237 HCC1569-EV and HCC1569-MCT2 cells (Fig. 5b).
238 Once tumours had reached 5 mm in diameter, mice were acutely dosed i.p. with either
239 MOG or IPOG at 100 mg/kg. At 2 hours post injection, mice were sacrificed and tumours were
240 collected. Analysis by LC-MS showed that the overall concentration of NOG in tumours from
241 mice dosed with IPOG was higher than in those dosed with MOG (Fig. 5c). Importantly,
242 tumours expressing MCT2 accumulated significantly more NOG when dosed with IPOG than
243 paired control tumours, whereas this was not the case in MOG-dosed animals.
244 Since there was no MCT2-specific accumulation of NOG in MOG-dosed animals, and
245 MOG is so rapidly converted to NOG in blood, we considered whether the observed NOG in
246 these tumours could be the result of direct NOG uptake. Indeed, it has been shown that NOG
247 is a substrate for the organic anion transporter OAT1[48], so to control for this possibility, we
248 also dosed animals with NOG directly. The concentrations of NOG in both EV and MCT2
249 tumours were similar to those dosed with MOG (Supplementary Fig. 2c, Fig. 5c), suggesting
250 that direct NOG uptake is likely the main source of NOG accumulation in this case, rather than

uptake of MOG itself. We can therefore infer that the increased stability of IPOG compared to MOG drives the increased NOG concentrations observed in MCT2-expressing tumours.

In addition to LC-MS analysis of NOG levels, we extracted metabolites from the paired, treated tumours and analysed them using gas chromatography mass spectrometry (GC-MS) metabolomics. Within the time-frame tested, there were minimal metabolic effects seen within the tumours after dosing with either compound, compared to the metabolic effects of MOG in cells[18]. Although there was a relative decrease in αKG and increase in αGP in MCT2-expressing cells upon IPOG dosing (which was not observed with MOG or NOG treatment) these changes were not statistically significant (Fig. 5d, Supplementary Fig. 3d).

Together, these data demonstrate that as a more stable pro-drug, IPOG enabled increased accumulation of NOG in MCT2-expressing tissues and could be used as a scaffold for further chemical iterations to develop additional prodrugs with improved utility as *in vivo* tool compounds.

DISCUSSION

Metabolism has far reaching effects on cellular physiology which extend beyond biomass accumulation, energy production and redox balance. A prototypical metabolite that illustrates this concept is α-KG; a central metabolic node which is not only the entry point of glutamine-derived carbons into the TCA cycle, but also a metabolite with important regulatory roles for key signalling proteins such as mTOR and HIF1α[8,15]. The effects of fluctuations in its concentration can be long lasting, with αKG also acting as a cofactor for DNA and chromatin modifying enzymes such as TET hydroxylases[9] and Jumonji demethylases[7], thereby influencing epigenetic processes within the cell. The αKG mimic NOG has been used to help understand many of the established roles of this important molecule. DMOG is a membrane-permeable, esterified analogue of NOG, which is rapidly de-esterified in cell culture media to the monocarboxylate MOG, a substrate of MCT2. The expression level of MCT2 determines the $[NOG]_{IC}$, which at high levels, inhibits a number of low affinity metabolic targets such as GDH and IDH, leading to toxicity in MCT2-expressing cancer cells[18].

Although DMOG continues to be used *in vivo*[49,50], it is dosed at very high concentrations, significantly beyond those required to inhibit intended targets *in vitro*[11]. Here, we show that DMOG and MOG are both rapidly converted to NOG in blood, each with a half-life of less than 5 minutes. We generated a series of analogues to improve the stability of MOG, allowing us to further increase its potential utility *in vivo*, while also exploring the structure-activity relationship of MCT2-dependent transport.

Insights into the MCT2 pharmacophore

As well as MOG, MCT2 transports endogenous monocarboxylates ranging from pyruvate and lactate to larger ketone bodies such as β-hydroxybutyrate, acetoacetate, α-ketoisovalerate and α-ketoisocaproate[51] (Supplementary Fig. 3) with a higher affinity than the other SLC16 family members[9]. Although less well studied, MCT2 plays important physiological roles including the uptake of astrocyte-secreted lactate into neurons within the brain [20,21]. MCT2 is highly expressed in some human cancers (Supplementary Fig. 4) and has been proposed as a biomarker for prostate cancer[22], as well as having pro-tumourigenic [23] and pro-metastatic roles[24] in breast cancer. A more detailed mechanistic understanding of this transporter could therefore open up new therapeutic opportunities, and provide the basis for further studies to generate *in vivo* imaging tools. By generating a series of MOG analogues, we therefore also aimed to further explore the structure-activity relationship (SAR) between MCT2 and its ligands, beyond what has been established based on endogenous substrates[51].

Interestingly, we observed very little tolerance for the α-methyl substitutions (**4**-**6**), all of which failed to meet our 2-fold threshold for MCT2-dependent uptake. These three analogues bare some structural similarity to α-ketoisocaproate (Fig. 1d, Supplementary Fig. 3), for which MCT2 has a K_m of 100 μM[51]. Their lack of transport therefore suggests that the combination of an α-methyl substitution with a carboxyl-ester group cannot be accommodated (Fig. 2c, d). Unexpectedly, we also observed no MCT2-dependent transport of the ketone analogue (**7**), potentially indicating that the oxygen in the MOG ester participates in an interaction with the substrate recognition pocket of MCT2 that is required for substrate binding and transport.

MCT2-dependent transport was maintained in the bulkier alkyl esters. We found that replacement of the methyl-ester leaving group with an ethyl-ester (**2)** was well tolerated by MCT2, with an almost eight-fold increase in uptake by MCT2-expressing cells compared to the control line. While transport was maintained with an isopropyl-ester substitution (**3**, IPOG), it occurred at a decreased level (a 2-fold increase in MCT2-expressing cells, Fig. 2d) indicating that the increased size led to some steric hindrance within the transporter.

The 5-membered aromatic heterocycles (**8**-**10**) were stable in blood (Supplementary Fig. 2a) and were also all transported in an MCT2-dependent manner with between a 2- and 4-fold enrichment in MCT2-expressing cells. Given the increasing interest in the role of MCT2 in cancer[52–54], this finding provides a useful set of scaffolds that could be built upon for the design of PET ligands to image MCT2 activity *in vivo.*

323 *Transporter-dictated effective concentration of compound determines target engagement*

324 Even in the case of very selective drugs, intracellular concentrations significantly
325 beyond those required to engage the intended target could lead to off-target effects and
326 toxicity. Here, we were able to demonstrate that transporter-mediated uptake heavily
327 influences compound efficacy and toxicity by determining intracellular concentration. Although
328 both the bulkier alkyl esters (**2**,**3**) are converted to NOG intracellularly, the $[NOG]_{IC}$ achieved
329 in MCT2-expressing cells varied widely (48.1, 16.4 and 4.65 mM for MOG, **2** and **3**
330 respectively), despite each analogue being dosed at the same concentration. The $[NOG]_{IC}$
331 achieved by each compound determined their effects within cells, reflected by their relative
332 impact on cell growth and apoptosis (Fig. 3a, b). PHD engagement by **2** and **3** was lower than
333 that by MOG based on the observed stabilisation of HIF1α (Fig. 3b). Similarly, compounds **2**
334 and **3** only partially inhibited reductive carboxylation, but they did not significantly suppress
335 the oxidative production of citrate (Fig. 3e) via inhibition of GDH[18]; as such only minimally
336 depleted TCA intermediates relative to that seen when dosing with MOG (Fig. 3c). Together,
337 our observations suggest that the decrease in proliferation that is observed with **2** and **3** is
338 modest because these compounds result in a $[NOG]_{IC}$ only sufficient to engage a subset of
339 the NOG targets that are collectively required for the maximal effects seen with MOG.
340

341 *Trade-off between blood stability and MCT2-dependent uptake*

342 The uptake of compound **2** into cells was higher than IPOG, however the ethyl-ester
343 substitution failed to improve its stability in blood relative to MOG. IPOG, on the other hand,
344 had a blood half-life more than four-fold higher than MOG. As a proof of principle, we were
345 able to show that its increased metabolic stability was sufficient to promote a significant
346 increase in NOG accumulation in MCT2-expressing tumours compared to control tumours
347 within the same animal (Fig. 5c). Therefore, while the MCT2-mediated uptake of IPOG
348 analogues would ideally be improved with further design iterations, IPOG, exemplifies a fine
349 balance between compound metabolic stability and MCT2 transporter-mediated uptake
350 towards future *in vivo* applications.
351

352 *Building new tools to probe αKG-dependent processes*

353 Given the extensive roles of αKG in cells, it is widely appreciated that NOG, as an αKG
354 mimic, is a promiscuous compound. Significant efforts have been made to generate tool
355 compounds and potential clinical leads to inhibit a number of its targets more selectively, in
356 particular the prolyl hydroxylases[11]. For other groups of αKG-dependent dioxygenases, there
357 are far fewer specific chemical inhibitors available. The TET enzymes are of particular interest,
358 given their well-established roles in regulating DNA methylation during early embryonic

359 development. More recently, it has become clear that they also enable cellular metabolic state
360 to impact upon epigenetic regulation[55,56] which can influence differentiation in cancer[16].
361 Isoform-specific TET inhibitors have yet to be developed, and so 'bump and hole'-based
362 approaches[57] have been employed to allow individual isoform targeting via engineered
363 enzyme isoforms with expanded active sites which can accommodate bulkier NOG
364 analogues[58]. The studies presented here could aid in the creation of cell-permeable
365 derivatives of these NOG analogues, enabling the study of specific TET enzymes both in cells
366 and potentially also *in vivo.*
367 Finally, although our analogue series were designed to mimic MOG to enable the study
368 of its MCT2-specific interactions *in vivo*, our findings could also be of use for the many labs
369 using DMOG as an *in vivo* tool more generally. Further development of IPOG with analogues
370 that also feature bulkier oxoacetate carboxyl ester groups will likely enhance blood stability
371 while maintaining general membrane permeability, improving the pharmacokinetic profile of
372 this tool compound.
373
374 **ACKNOWLEDGEMENTS**
375 We thank all members of the D.A. laboratory for valuable discussions and input throughout
376 this work, as well as members of the laboratory of L.F. for critical reading of the manuscript.
377 L.F.'s laboratory is funded by the MRC (MC-A654-5QC70). This work was funded by the MRC
378 (MC_UP_1202/1) and by the Francis Crick Institute which receives its core funding from
379 Cancer Research UK (FC001033), the UK Medical Research Council (FC001033) and the
380 Wellcome Trust (FC001033) to D.A. For the purpose of Open Access, the authors have
381 applied a CC BY public copyright licence to any Author Accepted Manuscript version arising
382 from this submission.
383
384 **AUTHOR CONTRIBUTIONS**
385 S.C. and D.H. designed (with input from L.F. and D.A.) and synthesised MOG analogues, and
386 advised on mouse dosing experimental design; P.N. performed orthotopic cell injections and
387 assisted with compound dosing in mice; N.B. assisted with cell line work; E.S. assisted with
388 and advised on compound stability measurements; M.S.d.S. and J.I.M. assisted with and
389 advised on metabolomics experiments; L.F. designed and performed all other experiments,
390 analysed and interpreted data. D.A. supervised the study, designed experiments and
391 interpreted data. L.F. wrote the first draft of the manuscript and developed it with support from
392 D.A. and input from S.C. and D.H. All authors reviewed and commented on the manuscript.
393
394

395 **MATERIALS AND METHODS**

396

397 *Chemical Synthesis*

398 Please see Supplementary Methods.

399

400 *Cell lines and cell culture*

401 HCC1569 cells were obtained from the American Type Culture Collection. Cells were cultured
402 in RPMI 1640 medium (Gibco, 31840) containing 10% fetal calf serum (FCS), 2 mM glutamine
403 and 100 U/ml penicillin/streptomycin, and were incubated in a humidified incubator at 37 °C
404 and 5% CO_2. All cell lines tested mycoplasma-free, and identity was confirmed by short-
405 tandem-repeat profiling (Francis Crick Institute Cell Services Science Technology Platform).
406 Generation of 'HCC1569-MCT2' over-expressing cells was achieved using retroviral
407 transduction of HCC1569 cells with a pBabe-puro vector containing the *SLC16A7* cDNA
408 sequence, as described previously[18]. 'HCC1569-EV' cells transduced with an empty pBabe-
409 puro vector were used as controls.

410

411 *Western blotting*

412 Cells on cell culture dishes were washed twice with PBS, before scraping in SDS sample
413 buffer (without beta-mercaptoethanol or bromophenol blue) and boiled for 5 min at 95 °C.
414 Protein was quantified using a BCA assay before adding beta-mercaptoethanol and
415 bromophenol blue and resolving by SDS–PAGE. Proteins were transferred to nitrocellulose
416 membranes by electroblotting, before blocking with 5% milk in Tris-buffered saline (50 mM
417 Tris-HCl, pH 7.5, and 150 mM NaCl) containing 0.05% Tween 20 (TBS-T). Membranes were
418 then incubated with the primary antibody overnight at 4 °C, washed with TBS-T and incubated
419 with horseradish peroxidase-conjugated secondary antibody for 1 h at RT in 5% milk TBS-T.
420 Antibodies were visualized by chemiluminescence and imaged using an Amersham
421 Imagequant 600 RGB.

422

423 Primary antibodies: HIF1α 1:500 (BD Biosciences 610958), MCT2 1:500 (generated by
424 Anastasiou lab). The secondary antibodies were as follows: goat anti–rabbit IgG conjugated
425 to HRP.

426

427 *Cell proliferation and apoptosis measurements*

428 Cell proliferation and apoptosis were measured in real time using an IncuCyteZoom (Essen
429 Bioscience). HCC1569 EV or MCT2 cells were seeded in 96-well plates at 9,000 cells per
430 well, in the presence of Incucyte Caspase 3/7 Green Apoptosis Assay Reagent (Essen
431 Bioscience). MOG analogues were added at doses indicated 16–20 h after seeding. Cells

432 were imaged (phase and fluorescence) at 3 h intervals, and automated image analysis was
433 used to determine confluence and number of apoptotic cells.
434
435 *Stable Isotope labelling and metabolite extraction for metabolomics*
436 Cells were seeded 1 day prior to the experiment in 6-cm dishes in RPMI medium (as described
437 above), containing dialysed FCS (3,500-Da MWCO). Medium was replaced with fresh at t = –
438 1 h. At t = 0, medium was replaced again to medium containing [U-^{13}C]-glutamine (2 mM) and
439 the MOG analogue of interest (1 mM) or 0.1% DMSO (vehicle control). Treatment/Labeling
440 was carried out for 4 h unless otherwise stated. Four or five technical-replicate plates were
441 used per condition and two or three additional plates of each cell line were counted to use for
442 normalisation of metabolite measurements. Cell diameter was also recorded for calculation of
443 cell volumes in order to determine intracellular concentrations. Cell diameter and number were
444 measured using a Nexcelcom Bioscience Cellometer Auto T4. At the end of the experiment,
445 plates were washed twice with ice-cold PBS, before quenching cells with the addition of 725 µl
446 dry-ice-cold methanol. Each plate was then scraped on ice, and samples were transferred to
447 a microcentrifuge tube containing 160 µl $CHCl_3$ and 180 µl H_2O (containing 2 nmol of scyllo-
448 inositol as an internal standard). Plates were scraped once more with an additional 725 µl of
449 cold MeOH, which was then added to the microcentrifuge tube containing the rest of the
450 sample. Samples were sonicated for 3 × 8 min in a water bath, and metabolites were extracted
451 overnight at 4 °C. Precipitated material was removed by centrifugation and samples were
452 subsequently dried and resuspended in 3:3:1 (vol/vol/vol) MeOH/H_2O/$CHCl_3$ (350 µl total), to
453 separate polar and apolar metabolites into an upper aqueous phase and lower organic phase,
454 respectively.
455
456 *Analogue uptake assays*
457 Cells were incubated with MOG or MOG analogues (1 mM) for 4 hours. Cells were then
458 washed with ice-cold PBS, and extracted as described for GC–MS above. Samples of the
459 polar phases were diluted 50-fold in 1:1 (vol/vol) MeOH/H_2O (containing 5 µM [U-^{13}C,^{15}N]-
460 valine as an internal standard) and analysed by LC–MS as described below.
461
462 *Gas Chromatography-Mass Spectrometry*
463 For GC–MS analysis, 150 µl of the aqueous phase was dried down in a vial insert, before
464 washing twice with 40 µl MeOH and drying again. Samples were methoximated (20 µl of
465 20 mg/ml methoxyamine in pyridine, RT overnight) before derivatising with 20 µl of N,O-
466 bis(trimetylsilyl)trifluoroacetamide + 1% trimethylchlorosilane (Sigma, 33148) for ≥1 h. An
467 Agilent 7890B-5977A GC-MS system was use to perform metabolite analysis. Splitless
468 injection (injection temperature 270 °C) onto a 30 m + 10 m × 0.25 mm DB-5MS + DG column

469 (Agilent J&W) was used, using helium carrier gas, in electron-impact ionization (EI) mode.
470 Initial oven temperature was 70 °C (2 min) with a subsequent increase to 295 °C at 12.5
471 °C/min, then to 320 °C at 25 °C/min (before holding for 3 min). Metabolite identification and
472 quantification was performed using MassHunter Workstation software (B.06.00 SP01, Agilent
473 Technologies) by comparison to the retention times, mass spectra and responses of known
474 amounts of authentic standards. Fractional labelling of individual metabolites is reported after
475 correction for natural abundance.
476
477 *Liquid Chromatography-Mass Spectrometry*
478 The LC–MS method was adapted from ref[59]. Samples were injected into a Dionex UltiMate
479 LC system (Thermo Scientific) using a ZIC-pHILIC (150 mm × 4.6 mm, 5-µm particle) column
480 (Merck Sequant). A 15-min elution gradient was used (80% solvent A to 20% solvent B),
481 followed by a 5-min wash (95:5 solvent A to solvent B) and 5-min re-equilibration; solvent A
482 was 20 mM ammonium carbonate in water (Optima HPLC grade, Sigma Aldrich) and solvent
483 B was acetonitrile (Optima HPLC grade, Sigma Aldrich). Flow rate, 300 µl/min; column
484 temperature, 25 °C; injection volume, 10 µl; and autosampler temperature, 4 °C. MS was
485 performed with positive/negative polarity switching using a Q Exactive Orbitrap (Thermo
486 Scientific) with a HESI II (heated electrospray ionization) probe. MS parameters: spray
487 voltage, 3.5 kV and 3.2 kV for positive and negative modes, respectively; probe temperature,
488 320 °C; sheath and auxiliary gases, 30 and 5 arbitrary units, respectively; full scan range, 70
489 to 1,050 m/z with settings of AGC target and resolution as 'balanced' and 'high' (3 × 106 and
490 70,000), respectively. Xcalibur 3.0.63 software (Thermo Scientific) was used to record data.
491 Prior to analysis, mass calibration was performed for both ESI polarities using the standard
492 Thermo Scientific Calmix solution. Calibration stability was enhanced by application of lock-
493 mass correction to each analytical run using ubiquitous low-mass contaminants. Parallel
494 reaction monitoring acquisition parameters: resolution, 17,500; auto gain control target,
495 2 × 105; maximum isolation time, 100 ms; isolation window, m/z 0.4; and collision energies,
496 set individually in high-energy collisional-dissociation mode. Equal volumes of each sample
497 were pooled to provide quality-control samples and were analysed throughout the run, thereby
498 providing a measurement of the stability and performance of the system. Xcalibur Qual
499 Browser and Tracefinder 4.1 software (Thermo Scientific) were used to perform qualitative
500 and quantitative analysis respectively, according to the manufacturer's workflows.
501
502 *Blood stability assay*
503 Blood was collected from euthanised NSG female mice into heparinised tubes, and used
504 immediately for experiments. To test stability, compounds were incubated at a final
505 concentration of 100 µM in blood (600 µL total volume), pre-warmed to 37 °C Samples were

506 collected in triplicate at 0 (compound added in to sample after extraction), 5, 15, 30 and 60
507 minutes. At the indicated time, 30 µl was taken and added to a tube on ice containing 100 µl
508 chloroform, 300 µl MeOH and 270 µl H_2O. [$U^{13}C$-^{15}N] valine was present in the aqueous phase
509 at a final concentration of 5 µM. Immediately after collection, samples were vortexed and
510 placed on ice. After all samples had been collected, they were sonicated for 3 x 8 mins and
511 incubated for 1h at 4 °C to allow extraction to proceed. Samples were then centrifuged (10
512 min, 4°C, full speed) and the aqueous phase transferred to a new tube, and stored at -80 until
513 they were ready to run on the LC-MS (Q Exactive) system, as described above. Samples were
514 quantitated against a 7-point standard curve of compound in mouse blood extract to minimise
515 matrix effects.
516
517 *Short term analogue dosing in vivo*
518 Adult female NSG mice were dosed by intra-peritoneal injection with MOG or MOG analogues
519 at 100 mg/kg. Blood samples were collected from the saphenous vein onto a Mitra micro-
520 sampling device (10 µl capacity, 100601-A, neoteryx) prior to injection (t=0) and at 15 minutes,
521 1h and 2h post injection. After two hours, dosed animals were euthanised by cervical
522 dislocation and tissues were harvested immediately and snap-frozen in liquid nitrogen before
523 storing at -80 °C. For blood samples, the micro-sampler 'sponge' tip was transferred into a
524 microfuge tube containing 33.3 µl CHCl3, 100 µl MeOH and vortexed thoroughly. [$U^{13}C$-^{15}N]-
525 valine was included to a final concentration of 5 µM in aqueous phase. Samples were
526 sonicated 3 x 8 mins at 4 °C in sonicating water bath and stored at -80 until required. Phases
527 were split by addition of 90 µl H_2O before spinning at 4 °C full speed for 5 mins (since MOG
528 analogues are susceptible to aqueous hydrolysis, H_2O was added immediately prior to
529 running). Aqueous phase was run on LC-MS as described above.
530 Extraction from tissues is described below.
531
532 *Orthotopic Xenograft assays*
533 6-8 week old female NSG mice were anaesthetised with 1.5-2% isofluorane (with oxygen),
534 and 1 million cells resuspended in Matrigel were injected into the mammary fat pad,
535 underneath the nipple. Two injections were carried out into mammary fat pads on opposing
536 flanks, using HCC1569 cells expressing an empty pBabe-puro vector ('HCC1569-EV') on one
537 side and pBabe-puro-MCT2 ('HCC1659-MCT2') on the other. Cells were tested for
538 mycoplasma and murine norovirus prior to injection. Tumours were monitored by palpation
539 and animal weight was measured twice per week. Length and width of tumours were
540 measured using callipers and volume calculated as 0.5*(length x width^2). Short-term dosing
541 experiments were carried out when tumours reached approximately 0.5 cm diameter.
542

543 All animal studies were ethically reviewed and carried out in accordance with Animals
544 (Scientific Procedures) Act 1986 and the GSK Policy on the Care, Welfare and Treatment of
545 Animals.
546
547 *Metabolite/drug extraction from tissue*
548 Snap frozen tissues were lyophilised and when dry (approx. 24h) they were ground in a pestle
549 and mortar. Powdered tissue was weighed out, and weight noted (~7 mg), so that after the
550 final biphasic extraction, samples can be diluted to ensure there are 2 mg/ 100 µl aqueous
551 phase. 600 µl 2:1 $CHCl_3$/MeOH was added to weighed tissue and vortexed thoroughly.
552 Samples were then sonicated in a sonicating water bath for 3 x 8 mins with 8 mins rest
553 between. Samples were spun full speed in microfuge for 5 mins to pellet insoluble material
554 and supernatant transferred to a new tube and dry down in a vacuum concentrator (with cold
555 trap). 600 µl 2:1 MeOH/H_2O was added to the remaining pellets and vortexed again.
556 Sonication (3 x 8 mins) was repeated before leaving to extract for at 4 for at least an hour.
557 Samples were then spun full speed in a microfuge for 5 mins to pellet insoluble material and
558 supernatant transferred to the tube containing the previous (apolar) supernatant, before drying
559 completely in a vacuum concentrator. Dried tubes can be stored at -80. A biphasic extraction
560 was then carried out on each sample (1:3:3 $CHCl_3$/MeOH/H_2O, 350 µl total) with aqueous
561 phase containing 5 µM [U-^{13}C-^{15}N]-valine as an internal standard, before vortexing thoroughly
562 and centrifuging at full speed, 4 °C for 5 mins to separate phases. For LC-MS analysis, the
563 volume of aqueous phase corresponding to 2 mg of dried tissue was added into a vial insert,
564 and made up to 100 µl with 1:1 MeOH/H_2O (with aqueous phase containing 5 µM [U-^{13}C-^{15}N]-
565 valine as an internal standard) so that equivalent tissue amounts are analysed. For GC-MS
566 analysis, *scyllo*-inositol was used as an internal standard, and samples were dried down after
567 biphasic before continuing with derivatisation as described for cell samples above.

568 **FIGURE LEGENDS**

569

570 **Figure 1 – Creating MOG analogues to improve blood stability**
571 **and explore MCT2 pharmacophore**

572 a) Schematic illustrating the conversion of DMOG to MOG, and subsequently NOG,
573 which is the active αKG analogue.
574 b) LC-MS analysis of DMOG stability in whole mouse blood over time. DMOG is very
575 rapidly converted to MOG, which is also unstable and subsequently forms NOG.
576 c) LC-MS analysis of synthetic MOG stability in whole mouse blood, table showing half-
577 lives of DMOG conversion to MOG and subsequently NOG.
578 d) MOG methyl ester replacement analogues. i) bulkier alkyl esters, ii) α-methyl
579 substituents, iii) ketone analogue, iv) 5-membered aromatic heterocycles.
580 e) Synthetic route for the preparation of MOG analogues 2-10.

581

582 **Figure 2 – MCT2-dependent uptake is maintained by alkyl ester**
583 **and aromatic heterocycle analogues**

584 a) Schematic to illustrate the cell system used to measure relative uptake of MOG
585 analogues: HCC1569 breast cancer cells transduced with either an empty pBabe
586 vector control (EV) or pBabe-MCT2.
587 b) Western blot demonstrating expression level of MCT2 in HCC1569-EV or HCC1569-
588 MCT2 cells.
589 c) Concentration of each of the analogues in EV or MCT2 expressing HCC1569 cells
590 after 4 hours of incubation with each analogue at 1 mM (mean ± SD).
591 d) Fold-change of analogue concentration in MCT2 expressing cells relative to EV cells.
592 A 2-fold increase (dashed line) was considered the threshold for MCT2-dependent
593 uptake (mean ± SD).

594

595 **Figure 3 – Analogues replicate MOG effects in cells in a NOG-dose-dependent manner**

596 a) Growth curves illustrating the dose-dependent effects of MOG analogues on cell
597 proliferation and apoptosis at different compound concentrations in either EV or MCT2-
598 expressing HCC1569 cells (mean ± SD).
599 b) Linear relationship between the inhibition of cell proliferation after treatment with 1 mM
600 of the indicated analogue (defined as the % increase in confluence at 96 h after
601 treatment, relative to untreated control cells, data from panel A) and the intracellular
602 NOG accumulated by that analogue. Error bars represent ± standard deviation.

603 c) Western blot showing the stabilisation of HIF1α after 4 hours of incubation with MOG
604 analogues in either EV or MCT2-expressing HCC1569 cells.
605 d) Schematic to demonstrate different routes of citrate synthesis and subsequent
606 labelling patterns from [U-^{13}C]-Glutamine.
607 e) Metabolic changes in EV or MCT2-expressing HCC1569 cells after 4 hours of
608 incubation with MOG analogues at 1 mM. Significance tested by multiple t-tests with
609 Holm-Sidak correction for multiple comparisons. (* = p< 0.05, ** = p< 0.01, *** = p<
610 0.001).
611 f) Labelling from [U-^{13}C]-Glutamine in EV or MCT2-expressing cells after 4 h of
612 incubation with analogues at 1 mM. M+4 citrate is derived from oxidative use of
613 glutamine carbons through the TCA cycle, whereas m+5 is formed as a result of
614 reductive carboxylation. Significance tested by multiple t-tests with Holm-Sidak
615 correction for multiple comparisons. (* = p< 0.05, ** = p< 0.01, *** = p< 0.001).
616
617 **Figure 4 – Increasing size of the alkyl ester substituent improves pharmacokinetics**
618 a) LC-MS analysis of MOG analogue stability in whole mouse blood over time (and
619 accumulation of NOG). Data points represent mean ± SD.
620 b) Concentration of MOG or compound **3** (IPOG) in blood at different time points after IP
621 injection at 100 mg/kg, and mean area under the curve (±SEM).
622
623 **Figure 5 – Compound 3 (IPOG) has improved MCT2-dependent uptake *in vivo***
624 a) Schematic illustrating orthotopic xenograft approach, in which HCC1569 cells
625 expressing either EV or MCT2 were injected into mammary fat pads on either flank of
626 the mouse to allow for paired analysis of uptake.
627 b) Growth rates of HCC1569 orthotopic xenograft tumours expressing either EV or MCT2
628 (no significant difference in growth, as determined by multiple t-tests at different time
629 points, with holm-sidak correction for multiple comparisons).
630 c) NOG accumulation in EV and MCT2 tumours 2 hours after 100 mg/kg IP injection with
631 either MOG or IPOG. Significance tested by paired t-tests. (* = p< 0.05)
632 d) Levels of α-ketoglutarate and α-glycerophosphate in EV and MCT2 tumours 2 hours
633 after 100 mg/kg IP injection with either MOG or IPOG. Significance tested by paired t-
634 tests.

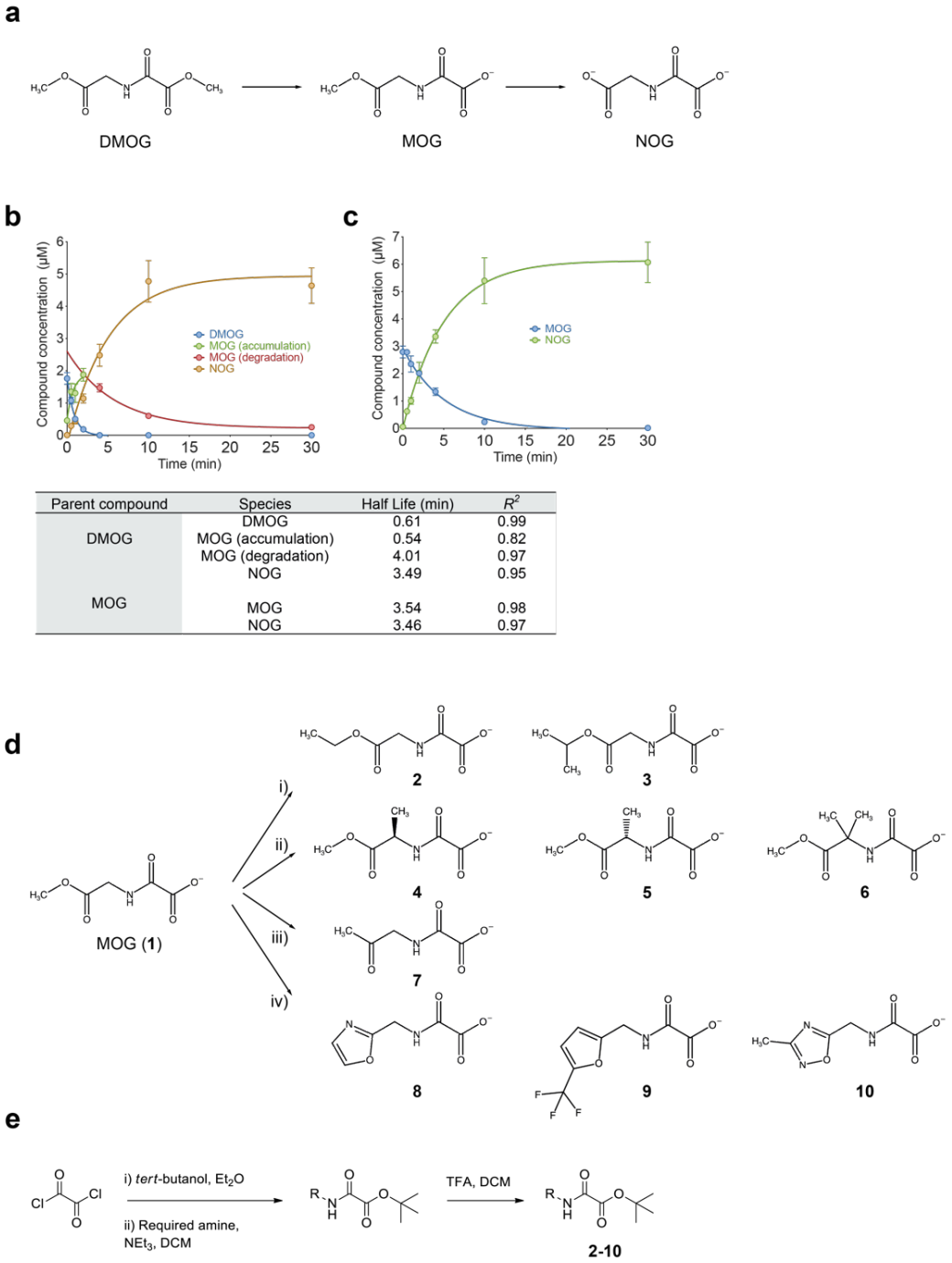

Parent compound	Species	Half Life (min)	R^2
DMOG	DMOG	0.61	0.99
	MOG (accumulation)	0.54	0.82
	MOG (degradation)	4.01	0.97
	NOG	3.49	0.95
MOG	MOG	3.54	0.98
	NOG	3.46	0.97

Fets *et al*; Figure 1

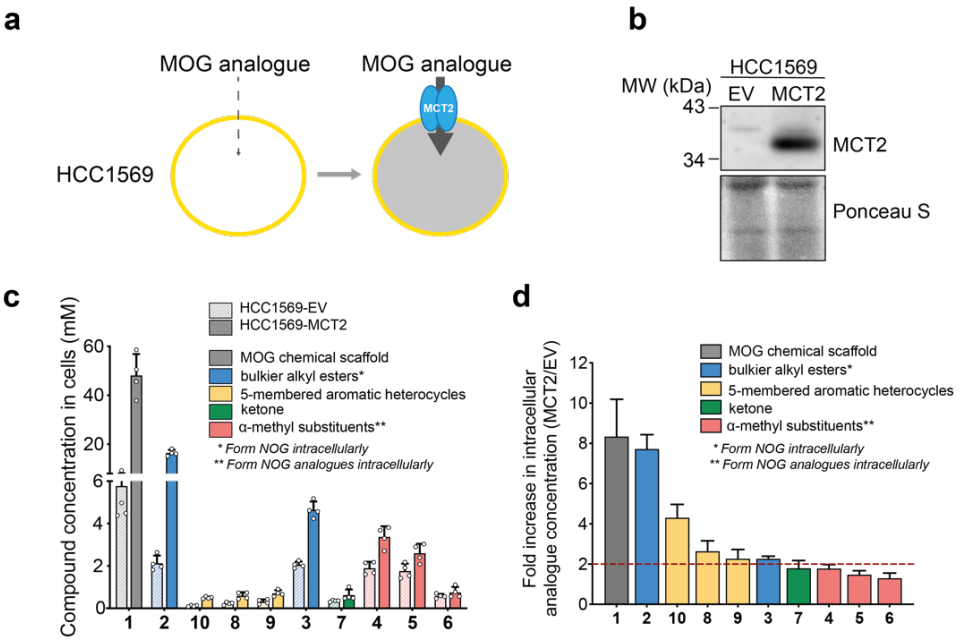

Fets *et al*; Figure 2

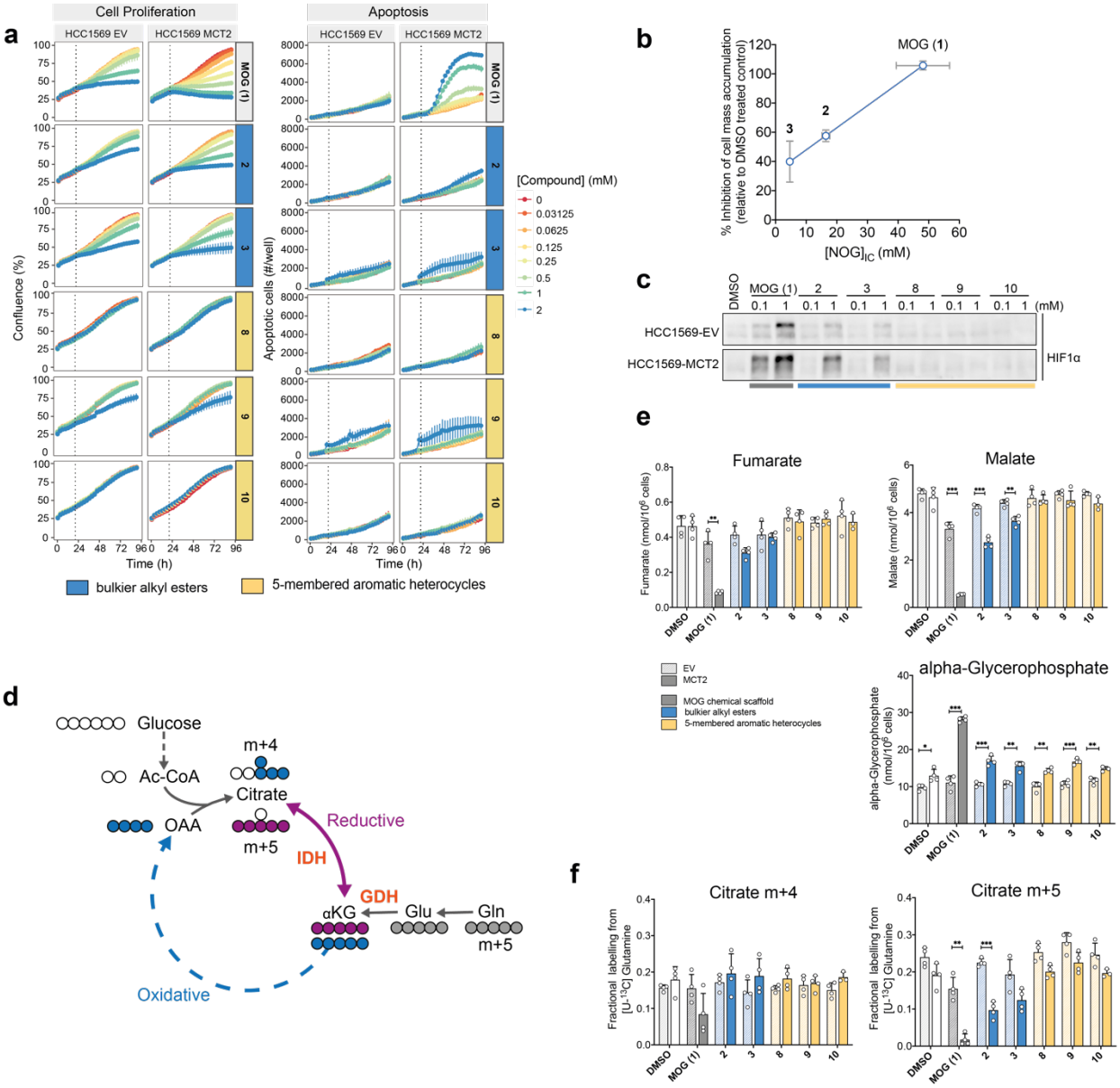

637

Fets *et al*; Figure 3

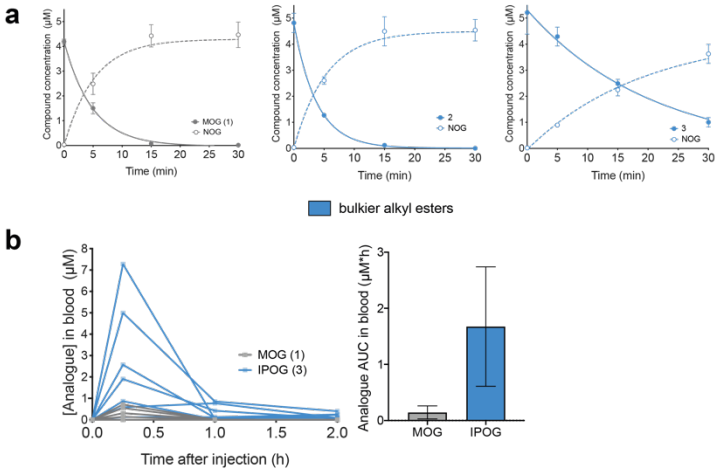

Fets *et al*; Figure 4

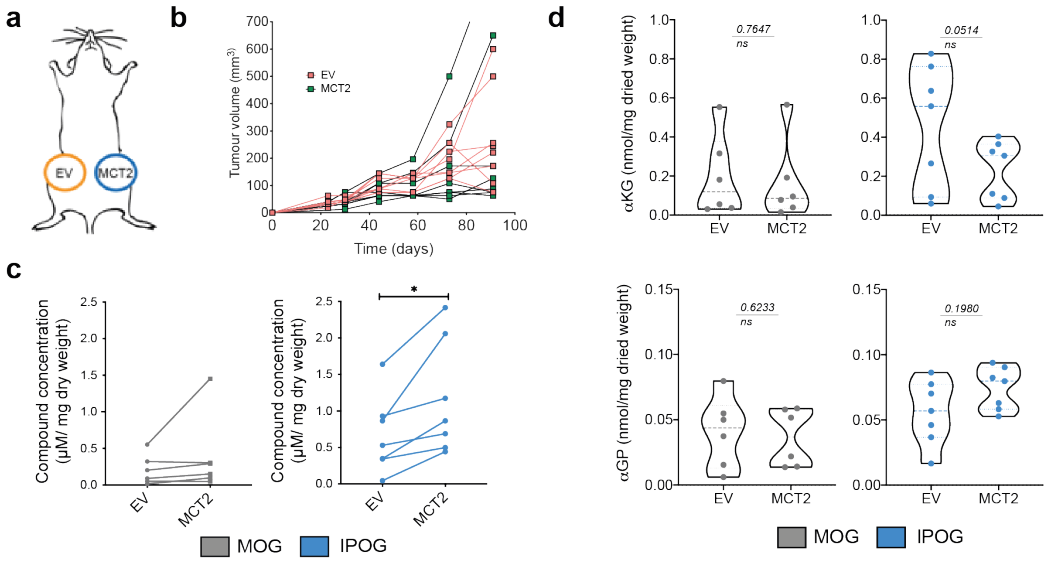

Fets *et al*; Figure 5

639

640 **SUPPLEMENTARY FIGURE LEGENDS**

641

642 **Supplementary Figure 1**

643 a) Levels of αGP in MCT2-expressing HCC1569 cells after 4 hours of incubation with
644 MOG analogues at 1 mM. Significance tested by ANOVA with Dunnet's test for multiple
645 comparisons, relative to DMSO control sample. (* = p< 0.05, ** = p< 0.01, *** = p<
646 0.001, **** = p< 0.0001).

647

648 **Supplementary Figure 2**

649 a) LC-MS analysis of MOG analogue stability in whole mouse blood over time (mean ±
650 SD).
651 b) Small scale analysis of NOG tissue distribution after IP injection of MOG or compound
652 3 (2h incubation, 100 mg/kg dose).
653 c) NOG accumulation in EV and MCT2 tumours 2 hours after 100 mg/kg IP injection with
654 NOG. Significance tested by paired t-tests. (* = p< 0.05)
655 d) Levels of α-ketoglutarate and α-glycerophosphate in EV and MCT2 tumours 2 hours
656 after 100 mg/kg IP injection with NOG. Significance tested by paired t-tests.

657

658 **Supplementary Figure 3**

659 Chemical structures of endogenous MCT2 substrates

660

661 **Supplementary Figure 4**

662 Ridge plots showing the range of expression levels of *SLC16A1* (MCT1), *SLC16A7*
663 (MCT2) and *SLC16A3* (MCT4) in different human cancer types. Data source: The Cancer
664 Genome Atlas, SKCM – Skin cutaneous melanoma; PAAD – Pancreatic Adenocarcinoma;
665 LUSC – Lung squamous cell carcinoma; LUAD – Lung adenocarcinoma; LGG – Low grade
666 glioma; GBM – Glioblastoma; ESCA – Oesophageal carcinoma; BRCA – Breast Invasive
667 Carcinoma.

668

669

a

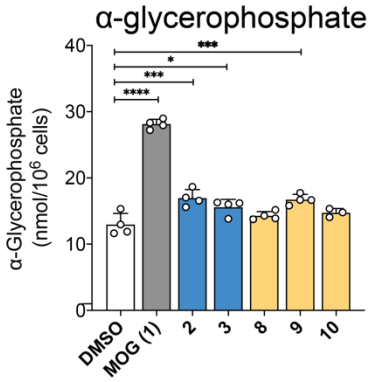

670

Fets *et al*; Suppl. Fig 1

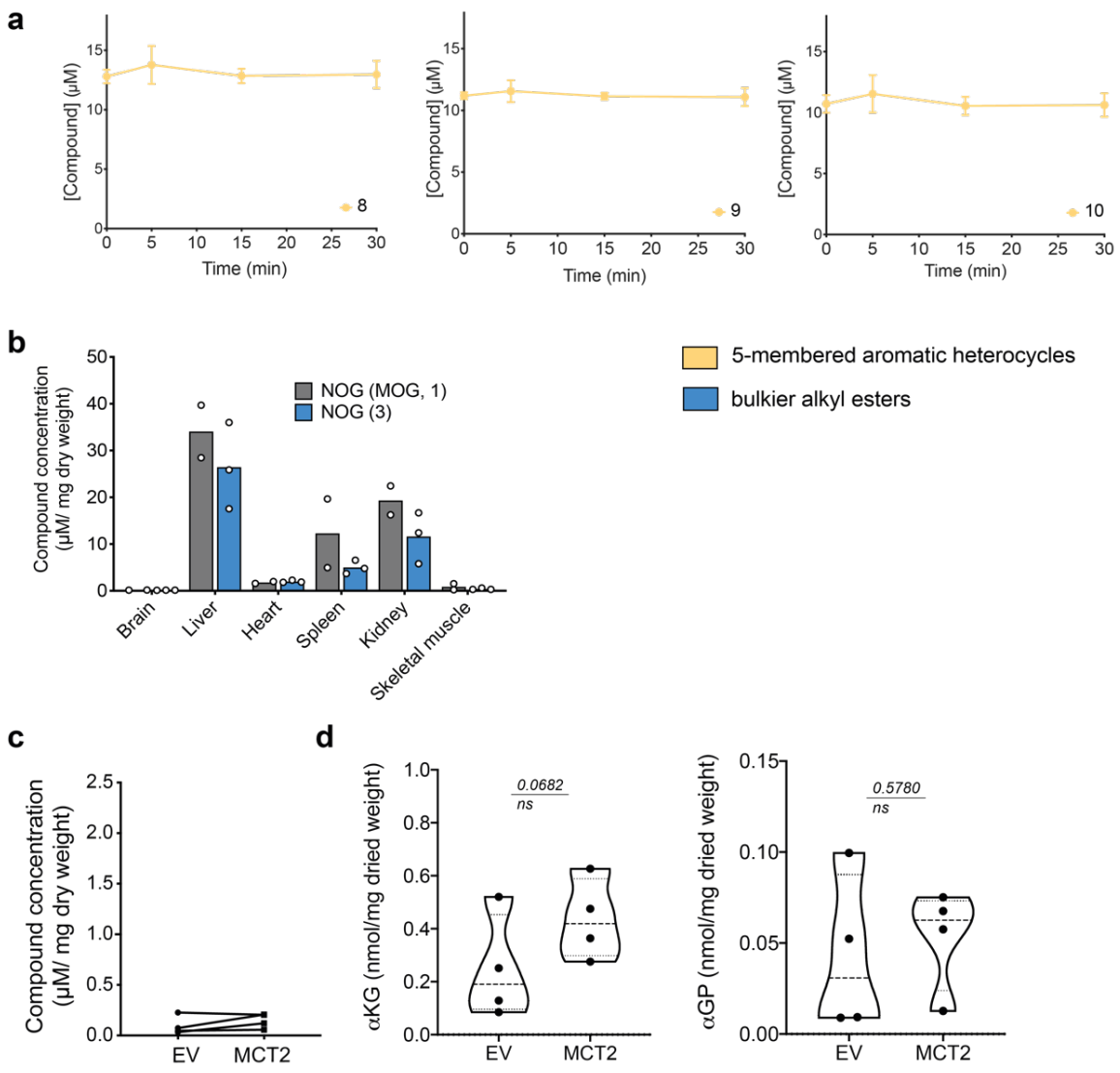

Fets *et al*; Suppl. Fig 2

671

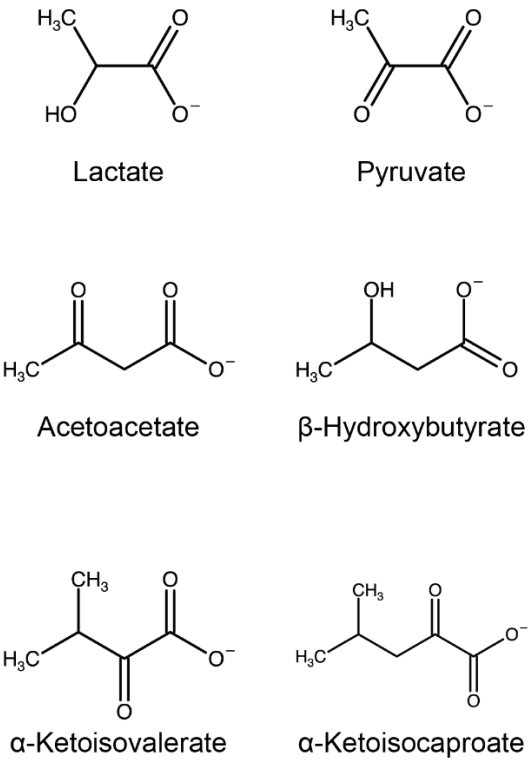

Fets *et al*; Suppl. Fig 3

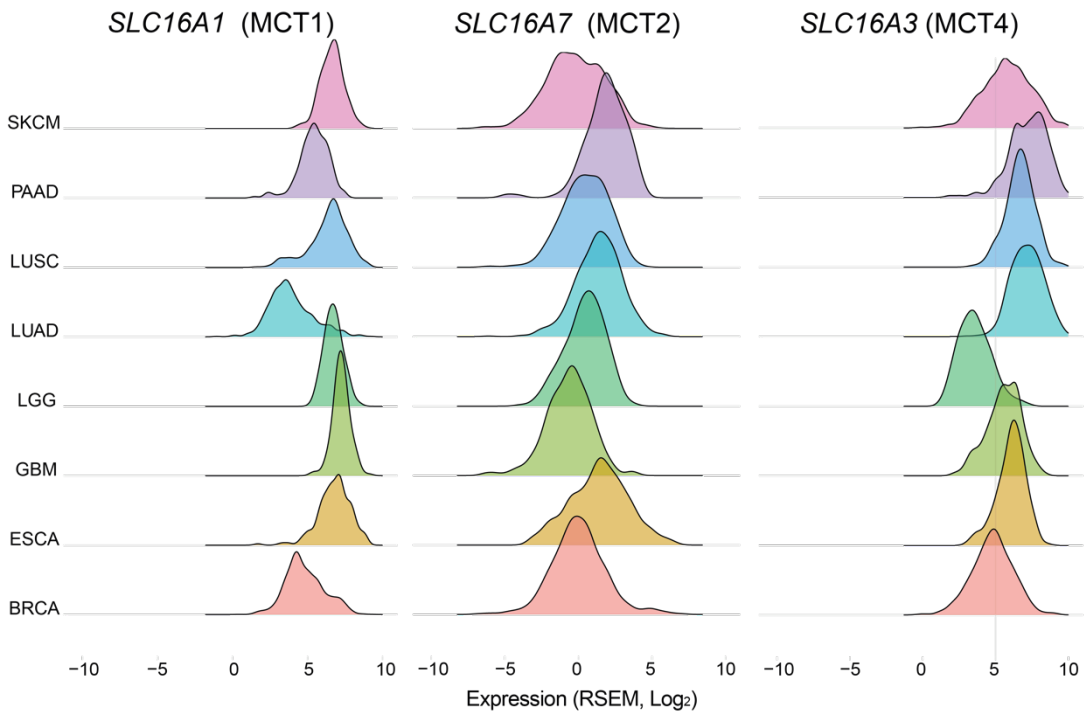

673

Fets *et al*; Suppl. Fig 4

674 **Supplementary Table 1.**

675 Mass spectrometry parameters for detection of MOG and MOG analogues

Compound Name/Number	m/z (negative mode)	Fragments	HCD
DMOG	174.0408	-	
NOG	146.0095	74.0245	35
1 (MOG)	160.0254	84.009, 59.013, 72.993, 100.004	35
2	174.0405	74.024, 84.009, 100.004	30
3 (IPOG)	188.0567	74.024, 84.009, 100.004, 85.029	30
4	174.0405	98.025, 114.020, 72.993, 59.013	30
5	174.0405	98.025, 114.020, 72.993, 59.013	30
6	188.0559	102.0559, 128.0354	30
7	144.0302	99.926	35
8	169.0255	68.014, 82.029	30
9	236.0171	135.0058,114.9996, 164.0323	30
10	184.0358	89.0429, 68.9955	30

676
677
678
679
680
681
682
683
684
685
686
687
688
689
690
691
692
693
694
695
696
697
698
699
700

701 **REFERENCES**

702 1. Woolley, D. W. The Revolution in Pharmacology. *Perspect Biol Med* **1**, 174–197 (1958).

703 2. Méndez-Lucas, A. *et al.* Identifying strategies to target the metabolic flexibility of tumours.
704 *Nat Metabolism* **2**, 335–350 (2020).

705 3. Liu, X. *et al.* Cystine transporter regulation of pentose phosphate pathway dependency and
706 disulfide stress exposes a targetable metabolic vulnerability in cancer. *Nat Cell Biol* 1–11
707 (2020) doi:10.1038/s41556-020-0496-x.

708 4. Lu, H. *et al.* Rational combination with PDK1 inhibition overcomes cetuximab resistance in
709 head and neck squamous cell carcinoma. *Jci Insight* **4**, e131106 (2019).

710 5. Luengo, A., Gui, D. Y. & Heiden, M. G. V. Targeting Metabolism for Cancer Therapy. *Cell*
711 *Chem Biol* **24**, 1161 1180 (2017).

712 6. Bobrovnikova-Marjon, E. & Hurov, J. B. Targeting Metabolic Changes in Cancer: Novel
713 Therapeutic Approaches. *Medicine* **65**, 157–170 (2014).

714 7. Hamada, S. *et al.* Synthesis and activity of N-oxalylglycine and its derivatives as Jumonji
715 C-domain-containing histone lysine demethylase inhibitors. *Bioorg Med Chem Lett* **19**,
716 2852–5 (2009).

717 8. Jaakkola, P. *et al.* Targeting of HIF-alpha to the von Hippel-Lindau Ubiquitylation Complex
718 by O2-Regulated Prolyl Hydroxylation. *Science* **292**, 468–472 (2001).

719 9. Amouroux, R. *et al.* De novo DNA methylation drives 5hmC accumulation in mouse zygotes.
720 *Nat Cell Biol* **18**, ncb3296 (2016).

721 10. Ivan, M. *et al.* HIFalpha Targeted for VHL-Mediated Destruction by Proline Hydroxylation:
722 Implications for O2 Sensing. *Science* **292**, 464–468 (2001).

723 11. Chan, M. C., Holt-Martyn, J. P., Schofield, C. J. & Ratcliffe, P. J. Pharmacological targeting
724 of the HIF hydroxylases – A new field in medicine development. *Mol Aspects Med* **47–48**,
725 54 75 (2016).

726 12. Eltzschig, H. K., Bratton, D. L. & Colgan, S. P. Targeting hypoxia signalling for the
727 treatment of ischaemic and inflammatory diseases. *Nat Rev Drug Discov* **13**, 852–869
728 (2014).

729 13. Cummins, E. P. *et al.* The Hydroxylase Inhibitor Dimethyloxalylglycine Is Protective in a
730 Murine Model of Colitis. *Gastroenterology* **134**, 156-165.e1 (2008).

731 14. Milkiewicz, M., Pugh, C. W. & Egginton, S. Inhibition of endogenous HIF inactivation
732 induces angiogenesis in ischaemic skeletal muscles of mice. *J Physiology* **560**, 21 26
733 (2004).

734 15. Duran, R. V. *et al.* Glutaminolysis Activates Rag-mTORC1 Signaling. *Mol Cell* **47**, 349 358
735 (2012).

736 16. Morris, J. P. *et al.* α-Ketoglutarate links p53 to cell fate during tumour suppression. *Nature*
737 1–5 (2019) doi:10.1038/s41586-019-1577-5.

738 17. Shahmirzadi, A. A. *et al.* Alpha-Ketoglutarate, an Endogenous Metabolite, Extends
739 Lifespan and Compresses Morbidity in Aging Mice. *Cell Metab* **32**, 447-456.e6 (2020).

740 18. Fets, L. *et al.* MCT2 mediates concentration-dependent inhibition of glutamine metabolism
741 by MOG. *Nat Chem Biol* **14**, 1 18 (2018).

742 19. Ogle, M. E., Gu, X., Espinera, A. R. & Wei, L. Inhibition of prolyl hydroxylases by
743 dimethyloxaloylglycine after stroke reduces ischemic brain injury and requires hypoxia
744 inducible factor-1α. *Neurobiol Dis* **45**, 733–742 (2012).

745 20. Nagamine, Y. *et al.* Inhibition of Prolyl Hydroxylase Attenuates Fas Ligand–Induced
746 Apoptosis and Lung Injury in Mice. *Am J Resp Cell Mol* **55**, 878 888 (2016).

747 21. Rautio, J. *et al.* Prodrugs: design and clinical applications. *Nat Rev Drug Discov* **7**, 255–
748 70 (2008).

749 22. Huttunen, K. M., Raunio, H. & Rautio, J. Prodrugs--from serendipity to rational design.
750 *Pharmacol Rev* **63**, 750–71 (2011).

751 23. Zawilska, J. B., Wojcieszak, J. & Olejniczak, A. B. Prodrugs: A challenge for the drug
752 development. *Pharmacol Rep* **65**, 1–14 (2013).

753 24. Jornada, D. *et al.* The Prodrug Approach: A Successful Tool for Improving Drug Solubility.
754 *Molecules* **21**, 42 (2015).

755 25. Stoeckel, K. *et al.* Stability of cephalosporin prodrug esters in human intestinal juice:
756 implications for oral bioavailability. *Antimicrob Agents Ch* **42**, 2602–6 (1998).

757 26. Barton, P., Laws, A. P. & Page, M. I. Structure–activity relationships in the esterase-
758 catalysed hydrolysis and transesterification of esters and lactones. *J Chem Soc Perkin*
759 *Trans 2* **0**, 2021–2029 (1994).

760 27. Talath, S., Shirote, P., Lough, W. & Gadad, A. Stability Studies of Some Glycolamide Ester
761 Prodrugs of Niflumic Acid in Aqueous Buffers and Human Plasma by HPLC with UV
762 Detection. *Arzneimittelforschung* **56**, 631–639 (2011).

763 28. JOHANSEN, M. & LARSEN, C. A comparison of the chemical stability and the enzymatic
764 hydrolysis of a series of aliphatic and aromatic ester derivatives of metronidazole. *Int J*
765 *Pharmaceut* **26**, 227–241 (1985).

766 29. Seki, H., Kawaguchi, T. & Higuchi, T. Specificity of Esterases and Structure of Prodrug
767 Esters: Reactivity of Various Acylated Acetaminophen Compounds and
768 Acetylaminobenzoated Compounds. *J Pharm Sci* **77**, 855–860 (1988).

769 30. Bender, D. M. *et al.* Cyclopropanecarboxylic Acid Esters as Potential Prodrugs with
770 Enhanced Hydrolytic Stability. *Org Lett* **10**, 509–511 (2008).

771 31. Tian, L. *et al.* Selective esterase-ester pair for targeting small molecules with cellular
772 specificity. *Proc National Acad Sci* **109**, 4756–4761 (2012).

773 32. Lavis, L. D. Ester bonds in prodrugs. *Acs Chem Biol* **3**, 203–6 (2008).

774 33. Yamazaki, Y., Kageyama, Y. & Okuno, H. Direct Evaluation of Stereoselectivity of Cancer
775 Esterases by Polyacrylamide Gel Electrophoresis Coupled with Activity Staining with Chiral
776 Naphthyl Esters. *Anal Biochem* **231**, 295–300 (1995).

777 34. Meanwell, N. A. Synopsis of Some Recent Tactical Application of Bioisosteres in Drug
778 Design. *J Med Chem* **54**, 2529–2591 (2011).

779 35. Nassar, A.-E. F., Kamel, A. M. & Clarimont, C. Improving the decision-making process in
780 the structural modification of drug candidates: enhancing metabolic stability. *Drug Discov*
781 *Today* **9**, 1020–1028 (2004).

782 36. BARLOW, R. B., BREMNER, J. B. & SOH, K. S. THE EFFECTS OF REPLACING ESTER
783 BY AMIDE ON THE BIOLOGICAL PROPERTIES OF COMPOUNDS RELATED TO
784 ACETYLCHOLINE. *Brit J Pharmacol* **62**, 39–50 (1978).

785 37. Patani, G. A. & LaVoie, E. J. Bioisosterism: A Rational Approach in Drug Design. *Chem*
786 *Rev* **96**, 3147–3176 (1996).

787 38. Diana, G. D. *et al.* Oxadiazoles as Ester Bioisosteric Replacements in Compounds Related
788 to Disoxaril. Antirhinovirus Activity. *J Med Chem* **37**, 2421–2436 (1994).

789 39. Street, L. J. *et al.* Synthesis and biological activity of 1,2,4-oxadiazole derivatives: highly
790 potent and efficacious agonists for cortical muscarinic receptors. *J Med Chem* **33**, 2690–
791 2697 (1990).

792 40. Bach, P. *et al.* 5-alkyl-1,3-oxazole derivatives of 6-amino-nicotinic acids as alkyl ester
793 bioisosteres are antagonists of the P2Y12 receptor. *Future Med Chem* **5**, 2037–56 (2013).

794 41. Brouwer, K. L. R. *et al.* In Vitro Methods to Support Transporter Evaluation in Drug
795 Discovery and Development. *Clin Pharmacol Ther* **94**, 95–112 (2013).

796 42. Yoo, H., Antoniewicz, M. R., Stephanopoulos, G. & Kelleher, J. K. Quantifying Reductive
797 Carboxylation Flux of Glutamine to Lipid in a Brown Adipocyte Cell Line. *J Biol Chem* **283**,
798 20621–20627 (2008).

799 43. Metallo, C. M. *et al.* Reductive glutamine metabolism by IDH1 mediates lipogenesis under
800 hypoxia. *Nature* **481**, 380 384 (2012).

801 44. Mullen, A. R. *et al.* Reductive carboxylation supports growth in tumour cells with defective
802 mitochondria. *Nature* **481**, 385 388 (2012).

803 45. Jiang, L. *et al.* Reductive carboxylation supports redox homeostasis during anchorage-
804 independent growth. *Nature* **532**, 255 258 (2016).

805 46. Rendina, A. R. *et al.* Mutant IDH1 Enhances the Production of 2-Hydroxyglutarate Due to
806 Its Kinetic Mechanism. *Biochemistry-us* **52**, 4563 4577 (2013).

807 47. Torres, C. M. *et al.* The linker histone H1.0 generates epigenetic and functional intratumor
808 heterogeneity. *Science* **353**, aaf1644 (2016).

809 48. Hagos, Y. *et al.* α-Ketoglutarate-related inhibitors of HIF prolyl hydroxylases are substrates
810 of renal organic anion transporters 1 (OAT1) and 4 (OAT4). *Pflügers Archiv - European J*
811 *Physiology* **464**, 367–374 (2012).

812 49. Kato, S., Takahashi, T., Miyata, N. & Roman, R. J. DMOG, a Prolyl Hydroxylase Inhibitor,
813 Increases Hemoglobin Levels without Exacerbating Hypertension and Renal Injury in Salt-
814 Sensitive Hypertensive Rats. *J Pharmacol Exp Ther* **372**, 166–174 (2019).

815 50. Dirscherl, K. *et al.* Hypoxia sensing by hepatic stellate cells leads to VEGF-dependent
816 angiogenesis and may contribute to accelerated liver regeneration. *Sci Rep-uk* **10**, 4392
817 (2020).

818 51. BRÖER, S. *et al.* Characterization of the high-affinity monocarboxylate transporter MCT2
819 in Xenopus laevis oocytes. *Biochem J* **341**, 529 (1999).

820 52. Pértega-Gomes, N. *et al.* Monocarboxylate transporter 2 (MCT2) as putative biomarker in
821 prostate cancer. *Prostate* **73**, 763 769 (2012).

822 53. Elia, I. *et al.* Breast cancer cells rely on environmental pyruvate to shape the metastatic
823 niche. *Nature* **568**, 1–5 (2019).

824 54. Huang, C.-K. *et al.* Adipocytes promote malignant growth of breast tumours with
825 monocarboxylate transporter 2 expression via β-hydroxybutyrate. *Nat Commun* **8**, 1
826 13 (2017).

827 55. Carey, B. W., Finley, L. W. S., Cross, J. R., Allis, C. D. & Thompson, C. B. Intracellular α-
828 ketoglutarate maintains the pluripotency of embryonic stem cells. *Nature* **518**, 413 (2015).

829 56. Schvartzman, J. M., Thompson, C. B. & Finley, L. W. S. Metabolic regulation of chromatin
830 modifications and gene expression. *J Cell Biol* **217**, jcb.201803061 (2018).

831 57. Islam, K. The Bump-and-Hole Tactic: Expanding the Scope of Chemical Genetics. *Cell*
832 *Chem Biol* **25**, 1171–1184 (2018).

833 58. Sudhamalla, B. *et al.* Complementary Steric Engineering at the Protein-Ligand Interface
834 for Analogue-Sensitive TET Oxygenases. *J Am Chem Soc* **140**, 1 7 (2018).

835 59. Zhang, T., Creek, D. J., Barrett, M. P., Blackburn, G. & Watson, D. G. Evaluation of
836 coupling reversed phase, aqueous normal phase, and hydrophilic interaction liquid
837 chromatography with Orbitrap mass spectrometry for metabolomic studies of human urine.
838 *Anal Chem* **84**, 1994–2001 (2012).